




Reliable determination of sub-nanometer gaps in plasmonic gold dimers for correlation to their optical properties

Francesca Scalerandi ¹, Alexander Skorikov ², Nathalie Claes ³, Sara Bals ³, Guillermo González-Rubio ⁴,
Nick Sokov ⁵ and Wiebke Albrecht ^{1,*}

¹*LMPV-Sustainable Energy Materials Department, AMOLF, Science Park 104, 1098 XG Amsterdam, The Netherlands*

²*Computational Imaging Group, Centrum Wiskunde and Informatica, Science Park 123, 1098 XG Amsterdam, The Netherlands*

³*EMAT and NANOLight Center of Excellence, University of Antwerp, Groenenborgerlaan 171, B-2020 Antwerp, Belgium*

⁴*Departamento de Química Física, Universidad Complutense de Madrid, Avenida Complutense s/n, 28040 Madrid, Spain*

⁵*Physical Chemistry, University of Konstanz, Universitätsstraße 10, Box 714, 78457 Konstanz, Germany*



(Received 28 March 2025; revised 16 July 2025; accepted 20 August 2025; published 10 October 2025; corrected 21 October 2025)

Accurately characterizing sub-nanometer gaps in plasmonic nanoparticle dimers is essential for understanding their optical properties, particularly in the transition from classical to quantum plasmonic behavior. While two-dimensional (scanning) transmission electron microscopy imaging provides high spatial resolution, it lacks the three-dimensional (3D) morphological information needed to reliably extract gap sizes. In this work, we combine electron tomography with a robust data analysis workflow to quantify interparticle gaps in gold nanosphere dimers with sub-nanometer precision. We show that gap size estimates are highly sensitive to reconstruction algorithms, segmentation thresholds, and meshing parameters. To overcome this, we introduce a model-fitting approach based on convolving a step function with a Gaussian, enabling consistent and accurate gap measurements even in the absence of a known ground truth. Validation on simulated datasets confirms pixel-level accuracy, and application to experimental data demonstrates the robustness and general applicability of the method. The resulting 3D reconstructions are directly integrated into electromagnetic simulations, allowing reliable interpretation of the optical response of the dimer. This workflow offers a broadly applicable strategy for correlating morphology and optical function in plasmonic systems and provides a crucial step toward resolving quantum effects in nanoscale light-matter interactions.

DOI: [10.1103/9jvw-qdsx](https://doi.org/10.1103/9jvw-qdsx)

I. INTRODUCTION

Plasmonic nanomaterials are versatile systems that can be employed in a large variety of different application fields [1]. They exhibit excellent performance in sensing tasks [2,3] and are utilized to sense single molecules [4,5]. They are employed as biomedical drug delivery [6,7] and hyperthermal cancer treatment agents [8,9]. Another important application field is photocatalysis, where plasmonic catalysts are used to enhance reaction rates and improve the selectivity of desired products [10–15]. The main reason for the success story of plasmonic nanosystems is their strong light-matter interactions due to localized surface plasmon resonances (LSPRs). These resonances are closely linked to the morphology and local surroundings of the nanoparticle (NP). This link makes the optical properties of plasmonic nanomaterials highly tunable [16]. For example, for single gold NPs, the optical

cross-sections span the visible-near-infrared (VIS-NIR) range when modifying the morphology [17,18]. Moreover, for typical sizes of plasmonic NPs, ranging from ~ 10 nm to several hundreds of nanometers, the optical cross-sections can be conveniently calculated by classical electrodynamics, allowing for an efficient morphology design process [19–21].

The story gets more complicated for smaller systems with sub-nanometer features, as quantum effects start to play a role [22]. In recent years, sub-nanometer control over the structure of plasmonic systems has therefore led to the field of quantum plasmonics [3,23–25]. In the spirit of the second quantum revolution, quantum plasmonics is exploited for the generation of nonclassical light for quantum information processing [26] and optoelectronic quantum plasmonic devices [27–29]. However, recent advances in nanofabrication and progress in measurement techniques have challenged our understanding of electrodynamics, as the local and linear assumptions used in the classical regime can no longer explain experimental observations. Consequently, the inclusion of nonlocal [30,31] and nonlinear [32–34] effects led to extended theoretical frameworks for mesoscopic electrodynamics [22]. The goal of these frameworks is to connect the more familiar classical electrodynamics with quantum physics [35,36].

A popular system to explore in the field of quantum plasmonics is a set of two plasmonic NPs with a specific distance

*Contact author: w.albrecht@amolf.nl

Published by the American Physical Society under the terms of the [Creative Commons Attribution 4.0 International](https://creativecommons.org/licenses/by/4.0/) license. Further distribution of this work must maintain attribution to the author(s) and the published article's title, journal citation, and DOI.

between them, known as plasmonic dimers [37]. An isolated spherical plasmonic NP displays one LSPR. In the case of a dimer, the two isolated resonances hybridize, resulting in an additional bonding dimer plasmon (BDP) mode at lower energies [38]. The BDP mode is excited when the polarization direction of the incoming light is parallel to the long axis of the dimer. This longitudinal mode is normally stronger than the transverse mode which, however, can still be excited and reflects the nature of the single particles. If the dimers are coupled not only capacitively but also conductively, a third mode related to charge movement over the whole structure arises: the charge transfer plasmon (CTP) mode [35,39–44]. The charge transfer then also affects the capacitive BDP mode, resulting in a blueshift of the BDP resonance [45,46], also referred to as *screened BDP* [39,44]. Such a blueshift of the BDP mode has in fact also been observed for non-touching dimers with sub-nanometric gap sizes [47,48]. This phenomenon has been attributed to quantum tunneling and has sparked a lot of interest in several communities. However, direct proof in the form of measuring the CTP mode is still lacking. Although a CTP mode for silver nanocubes conductively coupled through a molecular junction has been reported [49], the findings are debated in the community [50]. To the best of our knowledge, the interpretation of quantum tunneling has, therefore, mostly relied on a blueshifted and broadened BDP mode.

However, recent theoretical work on quantum electrodynamics challenges these interpretations. It has been shown that surface-enhanced Landau damping, also a quantum phenomenon but unrelated to charge transfer, might dominate instead, as it results in similar spectral shifts [51]. The question thus remains whether tunneling at optical frequencies occurs in these dimer systems or the optical response is rather dominated by a quantum-corrected surface response. In addition, the conductivity of the gap material needs to be considered as well [47]. Accurate correlations between measured and simulated cross-sections on a single dimer can help to answer these questions. In this manner, experimental results can be reliably compared with simulations including different quantum effects. To achieve this, however, the accurate morphology of the dimer systems needs to be known, particularly the gap size. Due to the sensitive response of LSPRs to any morphological changes, no unambiguous conclusions can be drawn otherwise. This is an underestimated bottleneck in the community, as normally no discussion occurs surrounding the error on the morphology and gap size. However, for quantum effects, even a gap size difference of 0.1 nm results in tremendous shifts of the BDP mode.

Although techniques like transmission electron microscopy (TEM) enable imaging down to atomic resolution, the task of precise gap-size determination is surprisingly nontrivial. The main limitation is that TEM provides two-dimensional (2D) projection images, whereas the physical world operates in three dimensions (3D). The gap between the particles can be distorted and therefore misestimated. Fortunately, reconstruction of the 3D morphology can be achieved through electron tomography (ET) [52–54]. ET is performed in standard TEM, where multiple 2D images are acquired from different projection angles by tilting the sample holder. To fulfill the projection requirement, ET is best performed

in high-angle annular dark-field scanning TEM (HAADF-STEM) mode for crystalline materials [53,55]. Since the limited space in TEM prevents the acquisition over the complete $\pm 90^\circ$ tilt range, ET suffers from the so-called missing wedge artifact, resulting in elongation and blurring in the direction perpendicular to the sample support plane. As a result, dedicated reconstruction algorithms were developed to reduce this information loss [56]. To create a shape as input for electromagnetic simulations, the reconstruction needs to be segmented to separate the dimer from the background and, depending on the simulation method, possibly turned into a surface mesh. All of the involved steps—i.e., the reconstruction, segmentation, and meshing—can lead to errors in estimating the dimer morphology. These inaccuracies can be minimized when using optimized workflows for the data processing pipeline. For example, we recently developed a workflow to generate an accurate surface mesh for single plasmonic NPs [20]. However, this problem is more challenging for dimers because their plasmonic properties are more sensitive to the morphology, especially of the gap region. An additional challenge is the finite pixel size of the 2D STEM data. Depending on the ratio of the needed field of view, i.e., the size of the plasmonic particles, and the gap size, the gap is often only represented by very few pixels.

In this work, we combine experiments and simulations to address the challenges of ET in reconstructing such (sub)-nanometer gaps in gold dimers. We begin by addressing the limitations of 2D STEM data for extracting reliable gap sizes. We particularly emphasize the challenges that emerge when defining segmentation thresholds, either in 2D or 3D. To solve the problem, we introduce a simple model for fitting sub-nanometer interparticle gaps in ET reconstructions of plasmonic gold NP-dimers. To verify our method, we apply it to simulated data with known sub-nanometric gap sizes. For the experimental ET data, the fit results allow us to choose the optimal threshold and meshing parameters to obtain the accurate 3D morphology, which can be used as input for electromagnetic simulations. We demonstrate that the developed workflow is independent of prior data treatment and, therefore, highly robust. We hope that our work encourages researchers to put more emphasis on extracting accurate morphological information on systems such as the small gaps in the gold dimers studied here. Since our developed strategy is applicable to any material, it provides an important stepping stone for determining quantum effects in plasmonic systems and beyond.

II. MATERIALS AND METHODS

A. Synthesis of gold NPs

1. Chemicals

All starting materials were used without further purification. Cetyltrimethylammonium chloride (CTAC, 25 wt. % in water), cetyltrimethylammonium bromide (CTAB), and hydrogen tetrachloroaurate trihydrate ($\text{HAuCl}_4 \cdot 3\text{H}_2\text{O}$, $\geq 99.9\%$) were purchased from Thermo Scientific. Silver nitrate (AgNO_3 , $\geq 99.0\%$) and L-ascorbic

acid ($\geq 99\%$) were purchased from Carl Roth. Milli-Q grade water (resistivity $18.2 \text{ M}\Omega \text{ cm}$ at 25°C) was used in all experiments.

2. Growth to 50 nm gold NPs

The 50 nm gold NPs were synthesized according to a recently reported method [57]. Briefly, 1 L of a 25 mM CTAC solution was prepared, and 10 mL of a 50 mM HAuCl_4 (0.5 mM) solution was added under stirring at room temperature. After 30 min, 4.5 mL of a 100 mM ascorbic acid solution was added to the mixture, which led to color change from yellow to pale yellow. In the next step, small volumes (25–50 μL) of the 100 mM ascorbic acid solution were added to reduce $\sim 99\%$ Au^{3+} ions to Au^+ . This process was monitored via the decrease in absorbance at 320 nm (i.e., corresponding to Au^{3+} -CTAC complex absorbance band maxima) until it reached a value close to 0.04 (cuvette of 1 cm path length). Then 600 μL of a 10 mM AgNO_3 solution (0.025 mM) and 174 μL of $9.5 \times 4.8 \text{ nm}$ gold nanorods ($[\text{Au}^0] = 7.9 \text{ mM}$; nanorods were synthesized according to a modified protocol described by González-Rubio *et al.* [58]) were used as seeds to trigger the formation of single-crystal gold NPs. The reaction mixture was stirred until 65°C was reached, the stirring magnet was removed, and the reaction vessel was left undisturbed in an oven at 65°C overnight. The reaction mixture turned red, indicating the formation of gold NPs. The synthesized NPs were centrifuged at 6600 rpm for 20 min and redispersed with a 2 mM CTAC solution. This step was repeated twice.

B. Nanodimers colloidal assembly

1. Chemicals

All starting materials were used without further purification. CTAB (96%), benzene 1,4-dithiol (BDT), and ethanol were purchased from Sigma-Aldrich. Milli-Q grade water (resistivity $18.2 \text{ M}\Omega \text{ cm}$ at 25°C) was used in all experiments.

2. Self-assembly of gold NPs

The gold NPs were colloiddally self-assembled using a modified protocol by Goppert *et al.* [59]. Here, $1.3 \times 10^{-8} \text{ M}$ of CTAB capped gold NPs, 50 nm in diameter, were used as a stock solution. Also, 139 μL of stock solution was diluted by adding 5 mM CTAB solution to 10 mL fresh Milli-Q water. Further, 425 μL of the obtained diluted gold NP solution was transferred to a glass vial and placed on a magnetic plate under continuous stirring at $\sim 400 \text{ rpm}$. Then 750 μL of Milli-Q water was added, followed by 10 μL of 5 mM CTAB solution and 340 μL of 10 mM BDT in ethanol. Additional ethanol was finally added to destabilize the CTAB capping agent and favor the ligand exchange. The reaction was quenched by the addition of 2 mL of 5 mM CTAB solution. The volume of added ethanol was varied, and the rate of agglomeration was followed in real time by ultraviolet-visible (UV-VIS) spectroscopy. Time-resolved UV-VIS spectra of the process can be found in Fig. S1 in the Supplemental Material [60]. The highest dimer yield was found for the addition of 350 mL of ethanol and waiting 12 min before quenching the reaction. Here, 20 μL of the solution just before quenching was dropcasted on a TEM grid previously cleaned by 10 min of

UV-ozone. The TEM grids used were 50 nm silicon dioxide membranes with nine windows of $100 \times 100 \mu\text{m}$ from SimPore.

C. Electron tomography

HAADF-STEM and ET were performed using an aberration-corrected Thermo Fisher Scientific Titan microscope, operated at 300 kV with a screen current of 42 pA. Images were acquired with a Fischione M3000 HAADF-detector using a convergence semiangle of 19.4 mrad and collection angles ranging from ~ 83 to 200 mrad. A camera length of 115 mm, magnification of $640\,000\times$, and pixel size of 137 pm were used. Images were acquired with a dwell time of 3 μs and a frame time of 4 s. For the ET experiments, images were acquired with α tilts from -66° to $+66^\circ$ with 2° steps. The electron beam was blanked in between successive acquisitions. The acquisition time for a full tomographic tilt series was $\sim 30 \text{ min}$. Subsequently, another tilt series (from -66° to $+66^\circ$ with 2° steps) for the same particle was acquired to investigate the stability over time and upon illumination by the electron beam. HAADF-STEM images before and after the acquisition of the tilt series were compared to evaluate possible damage caused by the electron beam.

D. Reconstruction of tomography data

As previously introduced, the 2D projections serve as input for reconstruction algorithms to retrieve the 3D shape. The acquired 2D projection images were first aligned using a cross-correlation-based algorithm. After alignment, the background was removed by subtracting the median of the intensity histogram, followed by detector shadowing and cupping artifact compensation. The cupping correction utilizes an algorithm based on Van den Broek *et al.* [61]. The corrected projections then serve as input for the reconstruction algorithms. In this work, two reconstruction algorithms were investigated: total variation minimization (TVM) and expectation maximization (EM). EM reconstructions were based on the implementation included in the ASTRA toolbox [62], and we used 15 iterations to avoid overfitting to noise [20]. TVM reconstructions were performed using the Chambolle-Pock algorithm with isotropic TV regularization, a non-negativity constraint and L2 data-error norm [63]. The algorithm was implemented based on GPU-accelerated primitives from the ASTRA toolbox [62] and PyTorch [64]. For these TVM reconstructions, the number of iterations was set to 1000, and the TV regularization weight was set to 3×10^{-4} . These parameters were optimized based on simulated reconstructions.

E. Simulation of STEM projections

To test our gap determination workflow, we simulated 2D HAADF-STEM projection images of a gold dimer system with a known gap size. To ensure that our simulated images closely resembled experimental STEM data, we accounted for inherent noise and imaging artifacts commonly present in electron microscopy. Key sources of artifacts include Gaussian blurring caused by defocus and astigmatism as well as Poisson noise, which arises due to the discrete nature of elec-

tron detection. Additionally, background signal contributions from the sample support were incorporated to create realistic STEM image simulations. The simulation flow is summarized in the scheme in Fig. S2(a) in the Supplemental Material [60]. The simulated STEM images were generated by forward projecting (c.2) a voxelized model of two gold NPs (c.1), each with a diameter of 50 nm and varying the gap distances, using the ASTRA toolbox (version 2.1.0) [62]. Gaussian blurring was applied to each projection using a Gaussian filter. Background signal levels were estimated from experimental data by analyzing the mean intensity of the sample support in HAADF-STEM images. This background was then added to the simulated projections. Finally, Poisson noise was introduced. The variance of the noise was manually optimized to match the noise level of experimental images. To validate the accuracy of the noise modeling in our simulated data, we compared line profiles from both simulated and experimental projections. As illustrated in Fig. S2(c) in the Supplemental Material [60], both line profiles show strong qualitative agreement, confirming the fidelity of the simulations. The small deviation arises because the simulation does not include the cupping artifacts present in the 2D experimental images. However, these artifacts are corrected during reconstruction; therefore, they do not represent a problem. Similarly, the histograms of the 3D reconstruction, shown in Fig. S2(b) in the Supplemental Material [60], display the same distribution. The differences in intensity are merely a matter of normalization.

In this manner, we simulated HAADF-STEM projection images of different dimer configurations: (1) using perfect spheres with a radius of 23 nm and gap varying between 1.09 and 0.55 nm; (2) a dimer with one sphere of 23 nm and the other of 30 nm in radius and a gap size of 0.82 nm; and (3) a dimer based on the voxelized experimental structure to account for asymmetric and not perfectly spherical particles with a gap of 0.68 nm. The somewhat arbitrary gap values chosen above resulted from the finite pixel size, for which we chose the same value as in the experiment (0.14 nm).

In this study, advanced TEM simulation methods, such as the multislice approach, were not employed, as our focus was not on atomic resolution imaging or quantitative image intensities.

F. Surface meshing of tomography data

We followed the workflow of Dieperink *et al.* [20] to generate a surface mesh from experimental and simulated ET data. Before segmentation, a Gaussian filter was applied to smooth the reconstruction. The degree of smoothing in terms of pixels, denoted by σ_{sm} , is provided throughout the text and varied from $\sigma_{\text{sm}} = 0$ (no smoothing) to $\sigma_{\text{sm}} = 4$. The smoothed reconstructions were then segmented using either the Otsu method or a fraction of the Otsu threshold value. Afterward, the voxelized structure was converted into a surface mesh using the marching cubes algorithm implemented in the scikit-image library [65,66]. Then to ensure a realistic computing time for electromagnetic simulations, the mesh needed to be simplified. We realized that the method used for mesh simplification made a critical difference for the reliability of the boundary element method (BEM) simulations.

For the dimers with sub-nanometer gaps, we found that the approximate centroidal Voronoi diagram (ACVD) algorithm performed best for mesh simplification. This method performs remeshing via Voronoi clustering, producing a more uniform distribution of triangles across the surface compared with other methods, such as the fast simplification algorithm, at the expense of potentially smoothing surface features. We applied this algorithm via the *pyacvd* module based on the work by Valette *et al.* [67]. We believe that the method works particularly well for the dimer case, as it favors uniform meshing, which is important to prevent numerical artifacts stemming from elongated mesh elements common in boundary and finite element method simulations. This is particularly important for the gap region, where only a few mesh elements significantly contribute to the overall optical response.

To demonstrate the difference in mesh simplification, we compare the quality of the meshes obtained using ACVD and the fast simplification algorithm for a simulated dimer in Figs. S3 and S4 in the Supplemental Material [60]. The meshing procedure was tested on the voxelized structure used as input for the STEM simulation, as explained in the previous paragraph. The resulting meshes from the different mesh simplification algorithms led to visibly different optical scattering spectra (Fig. S3 in the Supplemental Material [60]). We observed excellent overlap with the ground truth for the mesh simplified via ACVD, while a big discrepancy was observed for the fast simplification algorithm. The rather small gap difference (given in the legend in Fig. S3(a) in the Supplemental Material [60]) for the fast simplification mesh alone could not explain the significant deviation in optical response. This was confirmed by additional simulations using the extracted gap size and letting MNPBEM create its own mesh (blue lines in Fig. S3 in the Supplemental Material [60]). In this case, the overlap for the ACVD was excellent (dotted lines in Fig. S3 in the Supplemental Material [60]), but for the fast simplification method, the resonances differed by ~ 200 nm (dashed lines in Fig. S3 in the Supplemental Material [60]). This suggests that the fast simplification method introduces numerical inaccuracies due to a less homogeneous mesh. Furthermore, we noticed that the gap size after meshing as a function of segmentation threshold changed more smoothly for the ACVD method than the fast simplification method, both for the simulated (Fig. S4(a) in the Supplemental Material [60]) and experimental data (Fig. S4(b) in the Supplemental Material [60]). Plotting the mesh elements in the gap region indeed showed distorted mesh elements for the fast simplification method compared with the ACVD (Fig. S4(c) in the Supplemental Material [60]). Therefore, we believe that the ACVD mesh simplification is a more reliable method for the gold dimers, and for the rest of this work, we consistently use ACVD for mesh resampling. The target number of faces was set to 6000.

G. BEM optical simulations

The MATLAB MNPBEM toolbox was used to simulate the optical properties of gold dimers [21]. This method solves Maxwell's equations for objects with homogeneous and isotropic dielectric properties separated by sharp interfaces. In this method, only surfaces of the objects need to be

discretized, which leads to comparatively high convergence with low computational cost [20]. The inputs required for these simulations include the dielectric environment and the exact morphology of the object in the form of a surface mesh. In this work, the key parameters are the size and shape of the gold NPs and the gap size between them.

The dielectric constant of gold was taken from McPeak *et al.* [68]. For the surrounding medium, a constant refractive index of 1.334 was set. This value corresponds to the water immersion oil that we typically use in our experimental setup. The dimers were excited with a plane-wave with circularly polarized light propagating in the z direction. The scattering plots shown in Figs. 2 and 5 are plotted for only left circularly polarized light, whereas in Fig. 1 the sum of left- and right-circular polarization is plotted, which has only an influence on the intensity and not on the spectral dependence. A full (retarded) Maxwell's equations solver was used.

H. Convolution fit

To retrieve the gap size from the reconstructed dataset, we fitted a convolution of a Gaussian function and a step function to the extracted line profile. Equations (1) and (2) describe the Gaussian function and the step function, respectively, while Eq. (3) represents their convolution. In Eq. (1), A is the peak height of the Gaussian function, μ is the mean or center of the Gaussian distribution, representing the location of the peak. Here, σ_{fit} is the standard deviation of the Gaussian function, controlling its width. A larger σ_{fit} corresponds to a wider Gaussian, which in our case is related to the smoothing σ_{sm} that we applied to the reconstruction together with the experimental noise. Naturally, $\sigma_{\text{fit}} > \sigma_{\text{sm}}$, as shown in Fig. S5 in the Supplemental Material [60]. In the step function equation, Eq. (2), the parameters are the following: I_{HL} is the intensity on the left side of the gap before the step position, I_L is the intensity between the step positions in the gap area, I_{HR} is the intensity on the right side of the gap after the step position, and x_L^0 and x_R^0 are the positions where the step changes from one intensity to another and, therefore, the difference between them represents the gap size. Finally, the result of the convolution at position x represents the combined effect of the step and Gaussian functions.

The Gaussian was centered on the step function to ensure symmetric convolution around the transition point and avoid skewing from zero padding. To improve fit quality, the experimental data were interpolated and resampled to match the number of points in the Gaussian. The fitting process was then carried out using linear least squares minimization for σ , I_{HL} , I_{HR} , and I_L . The positions of the left and right steps were optimized using grid search, where the step function was shifted pixel by pixel across the data, and for each shift, a fit was performed. The fit with the lowest error was selected. To improve convergence, initial parameter estimates were obtained by independently fitting two logistic functions to either side of the gap, as shown in Fig. S6(c) in the Supplemental Material [60]. The inflection points of these logistic functions provided an estimate of the gap position, while the maximum and minimum on each side were used to estimate I_{HL} , I_{HR} , and I_L . A logistic function was chosen, as it is a sigmoid function with a qualitative behavior similar to the convolution

of a Gaussian and a step function. This similarity allows it to provide a good initial guess for the subsequent fitting step. Details of the initial parameters together with the constraints on their lower and upper boundaries used for the convolution fitting are summarized in Table S1 in the Supplemental Material [60]. The equations are as follows:

$$G(x) = A \frac{1}{\sqrt{2\pi}\sigma_{\text{fit}}} \exp\left[-\frac{(x-\mu)^2}{2\sigma_{\text{fit}}^2}\right], \quad (1)$$

$$S(x) = \begin{cases} I_{\text{HL}} & \text{if } x \leq x_L^0 \\ I_L & \text{if } x_L^0 < x < x_R^0 \\ I_{\text{HR}} & \text{if } x \geq x_R^0 \end{cases}, \quad (2)$$

$$(SG)(x) = \int_{-\infty}^{\infty} S(t)G(x-t)dt. \quad (3)$$

III. RESULTS AND DISCUSSION

A. 2D and 3D experimental data

The aim of this work is to establish a workflow for determining the size of a sub-nanometer gap between two (plasmonic) NPs with high accuracy, ideally on the order of the chosen pixel size, to simulate the optical properties of this dimer as precisely as possible. Figure S7 in the Supplemental Material [60] demonstrates why this is important. The presented simulated scattering spectra for gold dimers with a diameter of 50 nm highlight the strong dependence of the optical response on the exact size of the gap, particularly for sub-nanometer gaps. In the rest of the study, we focus on dimers of gold NPs separated by a bridge of organic ligands, in our case, the molecule BDT. This model system was chosen for two main reasons: (1) Gold is a very common plasmonic material and is stable under the electron beam, allowing us to test different acquisition parameters without the concern of electron beam-induced damage. (2) BDT exhibits a robust binding affinity to gold surfaces on both sides of its molecular structure due to the presence of thiol moieties, which facilitates the assembly of colloidal gold NPs into dimers. A solution of such dimers was prepared by introducing BDT into a solution of CTAB-capped gold NPs. Due to the stronger binding affinity of BDT than CTAB to gold surfaces, the native ligands were replaced by BDT, leading to the self-assembly of NPs into dimers (Au-BDT-Au dimers) with a yield $\sim 30\%$ (details in the Sec. II, Fig. S1 in the Supplemental Material [60]). For this system, we expected a gap size of ~ 0.6 – 0.9 nm, which is the size range of the BDT molecule length reported in the literature. Molecular mechanics force field calculations determined the length of the BDT molecule to be 0.846 nm when placed between gold atoms [69]. In another study, using chemistry drawing software, the length of a BDT molecule between two sulfur groups was determined to be 0.65 nm, whereas the length of a molecular junction of BDT between gold atoms was found to be 0.84 nm [70]. The exact gap size depends on the number and orientation of the BDT molecules in the junction. When a double layer of BDT forms, the gap was estimated to be 1.22 nm [71]. Additionally, from TEM images of gold nanocube dimers connected by BDT single-molecule junctions, a length of 0.67 nm was estimated [49].

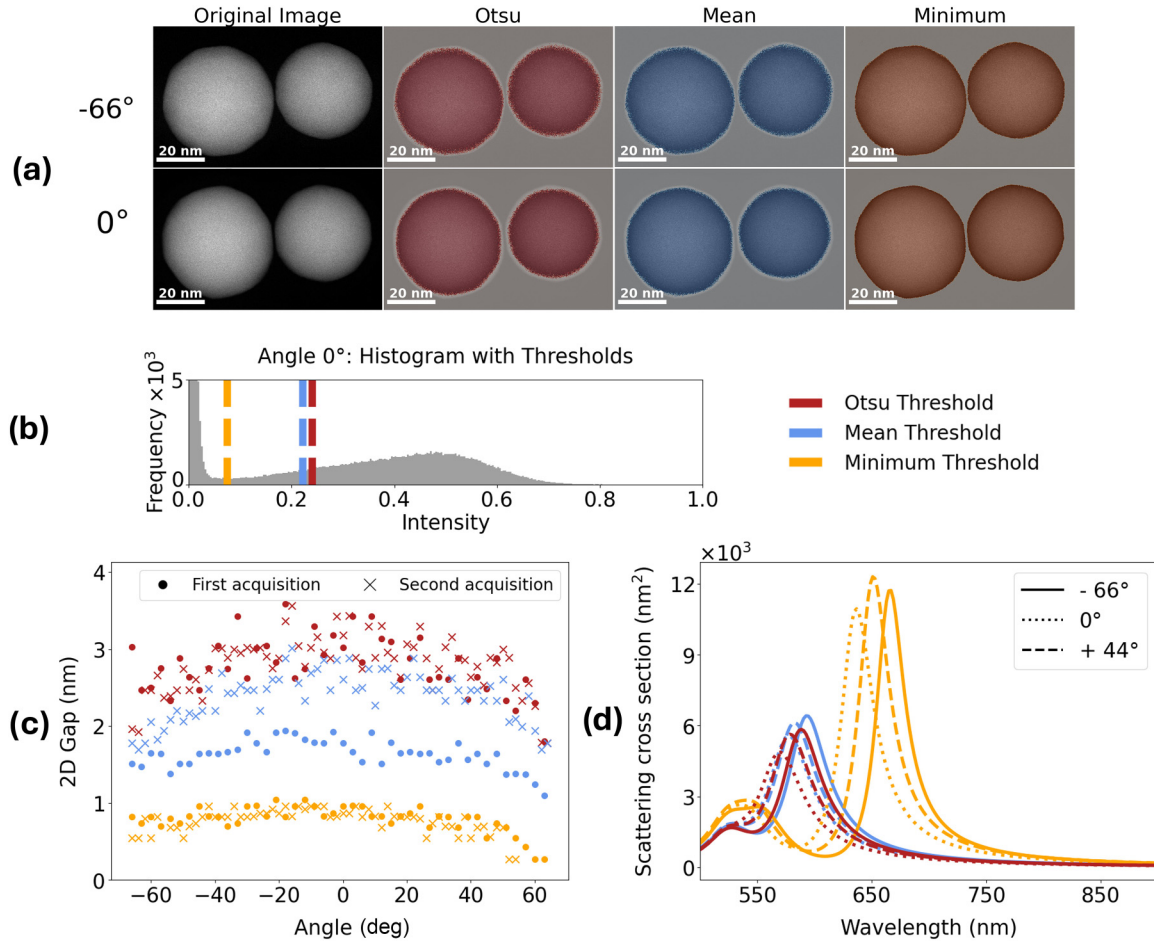


FIG. 1. Analysis of STEM images of two consecutive experimental tomography series of the same gold spheres dimer at tilt angles between $\pm 66^\circ$. (a) STEM images at two tilt angles, along with the corresponding binarized images overlaid: Otsu (red), mean (blue), and minimum (yellow). (b) Histogram of the STEM image at 0° , showing the threshold positions for the different binarization algorithms. (c) Extracted gap sizes from the binarized images for the three different threshold methods and two consecutive data acquisitions. (d) Simulated scattering spectra for the 3D shapes obtained from three representative angles and the different binarization algorithms.

To assess the gap size between particles, we began by analyzing 2D HAADF-STEM images taken at different holder tilt positions, i.e., along different viewing directions. Figure 1(a) shows two images captured at different angles for a representative dimer. Qualitatively, no significant difference can be observed between the two images taken along 0° and -66° . To extract the gap size for the investigated dimer from such 2D images, a conventional approach is to segment the particles by applying a global thresholding method. Subsequently, the gap can be determined in the resulting binary image. Global thresholding algorithms apply a single intensity threshold based on the intensity histogram of all pixels, thereby separating the foreground from the background. The threshold value determined depends on the chosen segmentation method. Here, we compare three popular algorithms: the minimum [72], mean [72], and Otsu [73] methods. The latter is defined as the value that maximizes the interclass variance in the intensity histogram. The mean method uses the mean intensity as a threshold value, whereas the minimum method selects the value corresponding to the minimum between the peaks in the intensity histogram. An example of a pixel intensity histogram and threshold position for the three methods is

shown in Fig. 1(b) for the HAADF-STEM image of the gold dimer at 0° .

Next, 2D HAADF-STEM images of the gold dimer with different tilt angles were segmented using the three described methods. In Fig. 1(a), the overlaid STEM and segmented images are shown. From this qualitative comparison, it is already obvious that this approach did not result in an accurate determination of the gap size. For the Otsu and mean thresholds, the segmented particles were clearly smaller than the particles in the STEM projection. For the minimum threshold, the opposite seemed to be the case. Figure 1(c) shows the problem quantitatively. Here, we extracted the gap between the particles based on the three different thresholding algorithms and for many projection angles (every 2° from -66° to 66°). The procedure to extract the gap was as follows: Once an image was segmented using one of the three segmentation methods, the gap was determined as the smallest distance between nonzero pixels using the exact Euclidean distance transform (EEDT). For each pixel in the segmented background, this function computes the shortest distance to the foreground segmentation. The smallest possible distance is then selected as the estimate of the gap size. An illustra-

tive representation of the process is sketched in Fig. S8(a) in the Supplemental Material [60]. Alternative methods such as fitting two circles and extracting the gap from the radius did not work since the particles were not perfectly spherical (Fig. S8(b) in the Supplemental Material [60]). As shown in Fig. 1(c), we obtained highly varying gap sizes ranging from 0.5 to 3.5 nm, although all of the analyzed images stemmed from the same gold dimer.

We conclude that 2D data are not suitable for reliably determining the gap size. One reason is that 2D STEM images are projection images, which overlook the 3D nature of the nanostructure. For example, if a dimer is not lying flat on the support, the projected gap would be different for different projection angles. However, for particles of similar size as in our case, which are expected to lie flat on the support, we believe that the dominant error factor stems from the segmentation methods. In fact, we recently showed that, even for simpler systems, such as single gold nanorods, these segmentation algorithms do not work reliably for 2D HAADF-STEM data [20]. The reason is that the thickness-dependent HAADF-STEM signal produces a rather skewed histogram without a clear separation between the foreground and background peaks, making it challenging to perform image segmentation [Fig. 1(b)]. Additionally, changes in background intensities, such as detector shadowing at high tilt angles or carbon contamination buildup, further influence the segmentation. This is likely part of the reason for the curved trend in Fig. 1(c) and the different results for different acquisitions on the same dimer [different symbols in Fig. 1(c)]. Ultimately, the inaccuracies in the estimated gap size makes it impossible to predict the optical properties of the gold dimer and prevents meaningful comparisons with spectroscopy data. We demonstrate this in Fig. 1(d), where we used the extracted gap sizes from Fig. 1(c) at three different angles for the three different segmentation methods and simulated the far-field scattering cross-sections for two spherical Au NPs with the corresponding gaps. Unsurprisingly, the spread in gap sizes resulted in significant shifts in the simulated scattering spectra, Fig. 1(d). The simulations were performed using the BEM, as implemented in the MNPBEM toolbox (more details in Sec. II C).

One way to overcome the segmentation limits for 2D HAADF-STEM data is by using ET. We have recently shown that 3D voxel histograms are better suited for segmentation tasks [20]. Therefore, we used the acquired tilt series presented in Fig. 1 as input to reconstruct the 3D morphology of the system. Indeed, also for the gold dimer system, performing a 3D reconstruction of the input projection images improved the separation of the foreground and background voxels (Fig. S9 in the Supplemental Material [60]). Voxel stands for *volume element* and represents the 3D equivalent of a pixel. It should be noted that we confirmed that the Au NPs did not change or move relative to each other under illumination by always acquiring two consecutive tilt series per dimer (Fig. S10 in the Supplemental Material [60]).

Although tomography helps with the segmentation process, extracting an accurate dimer gap size from the 3D dataset remains nonstraightforward. One of the first considerations in this process is the choice of an appropriate reconstruction method. We have recently shown that, for the reconstruction of metal NPs [20], TVM outperformed other common meth-

ods, such as the EM algorithm. TVM performed better in the case of isolated NPs because it utilizes prior knowledge about the smoothness of the object. EM, on the other hand, does not make use of prior knowledge about the object itself but only about the type of noise in the system, and it is particularly well suited for Poisson-distributed data such as STEM data. We compared both reconstruction algorithms for our dimer gap system. Details about the reconstructions can be found in Sec. II D. Slices through the middle of the two different reconstructions of the dimer from Fig. 1 are displayed in Fig. 2(a). The corresponding overlaid 3D visualizations are shown in Fig. 2(b). As expected, the TVM reconstruction outperformed EM in preserving the shape of the particles along the missing wedge direction (here, the z direction). However, since the TVM algorithm favors smoothness of the reconstructed object, we observed that the gap between the particles tended to get filled, resulting in a region of higher voxel intensities in the gap area, an effect not observed in the EM reconstruction. This is clearly demonstrated in the comparison of the line profiles shown in Figs. 2(a.3) and 2(a.4).

To extract the size of the gap from these reconstructions, they were segmented using the Otsu threshold method, which we found to be the most robust for ET reconstructions [20]. We anticipated that the gap size is significantly influenced by the noise in the reconstruction, which propagates into the segmentation. Given that the pixel size in the HAADF-STEM images and consequently the voxel size in the reconstruction were 0.14 nm, a 1 pixel difference due to noise artificially alters the gap size. Therefore, the data were smoothed using a Gaussian filter after reconstruction to reduce the local noise. We then applied the same EEDT as described above but now in 3D to extract the gap size from the segmented reconstructions. The results are presented in Fig. 2(c), showing the gap size as a function of the standard deviation for the Gaussian filter (σ_{sm}). When no data point is displayed for a particular σ_{sm} , it indicates that the segmentation resulted in the connection of the two spheres, and no gap could be identified. The same approach of smoothing the data could have also been explored for the 2D case. However, this work focuses on the 3D case, as it is more promising.

In Fig. 2(c), the spread in gap sizes was significantly reduced when using 3D reconstructions for segmentation rather than 2D HAADF-STEM images. However, the extracted gap size was influenced by the degree of smoothing applied to the reconstruction. For the TVM reconstructions (purple symbols), the extracted gap size decreased with increasing smoothing. That is expected since the TVM algorithm led to higher voxel intensities within the gap, enhancing the apparent connection between the spheres. As a result of smoothing, the gap size was further reduced. For the EM reconstructions, the extracted gap size started with a small value when no smoothing was applied and increased up to a smoothing level of 2, after which it decreased again. A likely explanation for this volcano trend is the following: Without smoothing, the extracted gap size was dominated by noise, resulting in an artificially small gap size due to misclassified voxels. Smoothing decreased the noise and therefore the influence of such misclassified voxels, resulting in a larger gap size. Of course, for stronger smoothing (and our voxel size of 0.14 nm), the gap decreased again due to blurring effects.

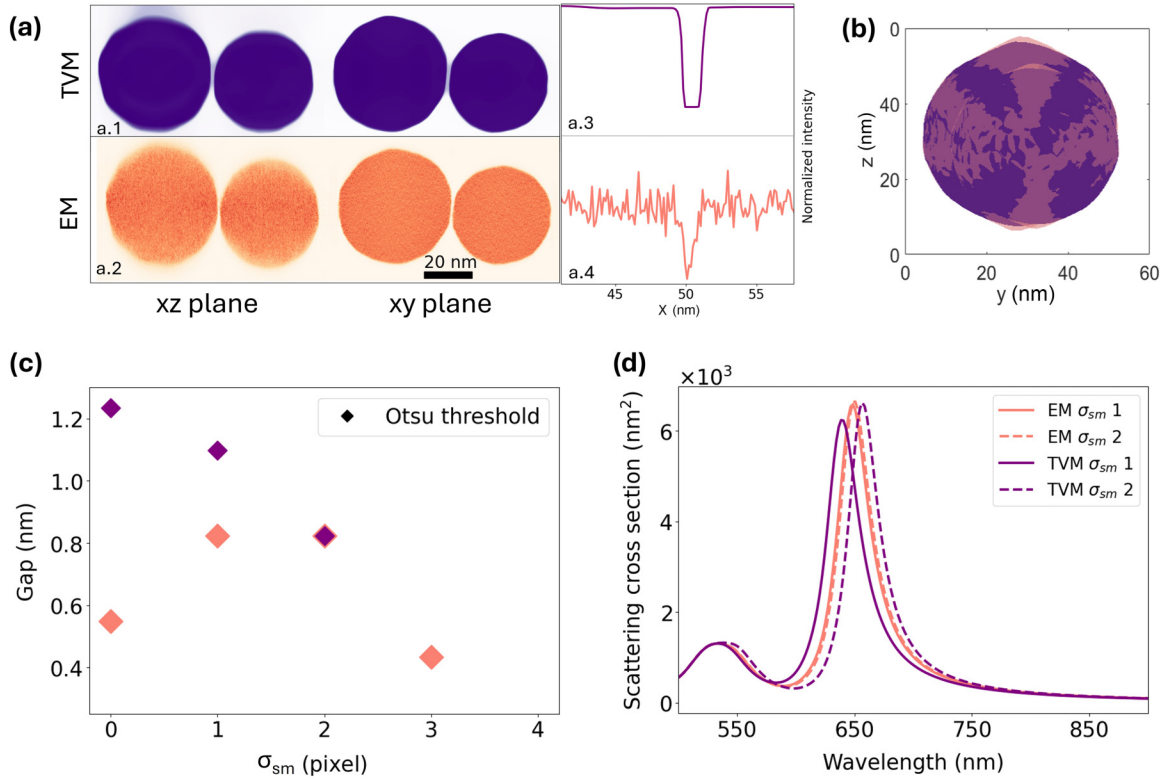


FIG. 2. Analysis of experimental ET data obtained from the same gold dimer as shown in Fig. 1. (a) Slices along the xz plane and xy plane of 3D reconstructions obtained by (a.1) TVM (purple) and (a.2) EM (salmon) algorithms. Corresponding line profiles along the gap in the x direction are shown for the TVM and EM reconstructions in (a.3) and (a.4), respectively. (b) The BEM mesh input is visualized across the yz plane, with meshes obtained from the EM (salmon) and TVM (purple) reconstructions overlaid in a semitransparent manner. (c) The extracted gap from each reconstruction is shown. The gap is defined as the smallest Euclidean distance between the two particles after binarizing the data using Otsu's thresholding method. The reconstructions were smoothed with different values of σ_{sm} before segmentation. (d) Simulated scattering spectra using the mesh obtained from EM and TVM reconstruction smoothed with $\sigma_{sm} = 1$ and 2 as input.

Ultimately, to link a specific geometry of the dimer system to, e.g., optical measurements, electromagnetic simulations of the optical properties need to be performed. The BEM method that we used in Fig. 1 can also be applied to the 3D case, keeping in mind that the BEM method requires a surface mesh of the 3D system as an input. This can be done in two manners: (1) approximation through a model system using perfect spheres and (2) direct surface mesh generation from the input tomography data. The first approach involves using the extracted gap size, Fig. 2(c), and the radius obtained by fitting two spheres to the voxelized data. Although it is simpler and computationally efficient, this method does not capture deviations in particle morphology. The NPs are rarely perfect spheres and, in our case, surface facets can indeed be seen in Fig. 2(a). The nonspherical geometry also led to artifacts when approximating the sphere diameter and sometimes to overlapping spheres for small gap sizes, see Fig. S8(b) in the Supplemental Material [60]. Therefore, we recommend the second approach, which involves creating a surface mesh directly from the 3D tomographic reconstruction. Although it is significantly more challenging, this approach is more accurate, as it incorporates the actual morphology of the investigated NPs. We followed the workflow of Dieperink *et al.* [20]. First, we segmented the reconstruction. Related to the discussion surrounding Fig. 2(c), we compared $\sigma_{sm} = 1$ and 2, using the Otsu method for thresholding. The segmented data

were then transformed into a surface mesh with a low enough number of faces to perform the BEM simulations in a reasonable time. To achieve this, a combination of the marching cube and ACVD mesh simplification algorithms was used, as detailed in our previous work and Sec. II F [20].

In Fig. 2(d), simulated scattering spectra, using the morphology of the mesh structure obtained from EM and TVM reconstructions after applying Gaussian smoothing of 1 and 2 as input, are displayed. Although less spread than for the 2D case, differences in the simulated spectra for the different reconstruction methods and smoothness can be observed. We attribute these differences to three main factors: (1) variations in the extracted gap size after segmentation [as displayed in Fig. 2(c)], (2) modifications of the gap size due to mesh simplification, and (3) deviations in the reconstructed NP morphology, Fig. 2(a). All of these effects are intertwined. From Fig. 2(b), we know that the gap size differs by ~ 0.3 nm between the TVM- and EM-based Otsu-segmented reconstructions for $\sigma_{sm} = 1$. A blueshift in the scattering spectrum is expected for an increasing gap size. Indeed, the scattering spectrum obtained from the TVM reconstruction was blueshifted [solid purple line in Fig. 2(d)] compared with the EM reconstruction (solid salmon line). The main difference for $\sigma_{sm} = 1$ was therefore likely dominated by factor (1). However, quantitatively, we would expect a larger blueshift for a gap-size difference of 0.3 nm, indicating that the other

factors also play a role. The case was even more complex for $\sigma_{\text{sm}} = 2$, as the gap measured after segmentation was the same for the two Otsu-segmented reconstructions, Fig. 2(b), yet the simulated scattering spectra differed [dashed lines in Fig. 2(c)]. In this case, factors (2) and (3) seem to have caused the observed differences.

It is important to note that mesh simplification unavoidably introduced small deviations in the morphology of the dimer. Since the scattering response of dimers is highly sensitive to sub-nanometer variations in the gap size, these morphological differences can significantly impact the final results. To better understand the influence of mesh simplification, we extracted the gap sizes at the two different stages of the pipeline [Fig. S11(a) in the Supplemental Material [60]]: after segmentation (in voxel space) and after mesh simplification. We observed that mesh simplification led to a slightly smaller gap for the TVM reconstructions, whereas the gap for the EM reconstructions increased. This effect reduced the difference in apparent gap size for $\sigma_{\text{sm}} = 1$, explaining the unexpectedly small spectral difference in Fig. 2(d). For $\sigma_{\text{sm}} = 2$, meshing resulted in a smaller gap of the TVM reconstruction, supporting the observed redshift compared with the EM reconstruction. It is important to note that the quality of the mesh after mesh simplification played a critical role in achieving reliable electromagnetic simulations, as detailed in Sec. II F. Due to the small features in the gap region that dominate the optical response for these dimers, it is important to avoid distortions and significant size differences in the mesh faces (Figs. S3 and S4 in the Supplemental Material [60]).

Next to differences in gap size, changes in morphology can also contribute to the observed differences in the simulated scattering spectra [factor (3)]. ET is well known to suffer from the so-called missing wedge artifact. This artifact stems from the physical constraint in the pole piece gap of an objective lens, which limits the tilt range of holders. For an ideal reconstruction, a tilt range of $\pm 90^\circ$ would be required, which is not achievable in practice. The missing angular information results in blurring and lemon-shaped artifacts perpendicular to the sample support plane. This can be clearly seen in the xz slices through the reconstruction shown in Fig. 2(a). The effect is more drastic for the EM reconstruction because the prior knowledge used in TVM helps to suppress these artifacts effectively. The overlay of both reconstructions after meshing in Fig. 2(b) clearly shows a pronounced elongation in the z direction for the EM reconstruction (salmon). This also resulted in a slightly larger volume of the EM reconstructions compared with the TVM ones (Fig. S11(b) in the Supplemental Material [60]). Finally, to investigate how the elongation caused by the missing wedge influences the simulated optical properties, scattering spectra were simulated for different gap sizes and varying ellipticities of the particles (Fig. S12 in the Supplemental Material [60]). We observed that the missing wedge effect, manifesting itself as an elongation along the z direction, would lead to a small redshift of the gap plasmon resonance. These results suggest that factor (3) influenced the simulated scattering spectra the least compared with factors (1) and (2).

Together, all three factors explain the differences in the simulated scattering spectra. Figure 2, therefore, tells us that only a good combination of smoothing and segmentation re-

sults in the correct size of the gap and accurate simulated scattering spectra. However, for experimental data, these parameters are unknown. Rather than relying on the combination of the optimal parameters for smoothing and segmentation, one would ideally apply a method that can determine the gap size while being insensitive to the values of any processing parameters like smoothing. If the gap can be reliably determined, then the segmentation and meshing can be adjusted to ensure the determined gap size is preserved. In the following, we propose a procedure to precisely determine the interparticle gap, allowing us to minimize these uncertainties for the experimental data.

B. Simulated data and convolution method

The challenge in evaluating the experimental data presented in Figs. 1 and 2 is that the exact size of the gap is unknown. To address this issue, we simulated ET data for dimers of gold NPs with known varying interparticle gap sizes. Details about the procedure of these simulations are given in Sec. II E. The same workflow as for the experimental series above was used to reconstruct the 3D morphology from the simulated tilt series. In the above section, it became evident that the choice of data processing pipeline is crucial for the final gap size estimation, even with ET data. To address this issue, we developed a robust model to retrieve the gap size through fitting of the ET data. Fitting is always an elegant solution to extract quantitative information, as it incorporates the knowledge about the physical system. In our case, we extracted line profiles along the direction of the gap for the central slice of the reconstruction. We then fitted the line profiles on the basis of the following assumptions. In a slice through a 3D reconstruction, the intensity is not a function of thickness, as is typically the case for 2D HAADF-STEM images. Therefore, in the ideal case, without any type of noise or image artifacts, the gap would look like a perfect step function. However, 3D reconstructions are affected by different artifacts, primarily microscope aberrations and image series misalignment, whose combined effect can be approximated by Gaussian-shaped point spread function [74]. Based on this, we propose fitting the line profile along the gap of the reconstruction using a convolution of a step function and a Gaussian blur kernel. This approach allows the gap size to be extracted from the step function component. The underlying workflow is described in the following.

The first step in the workflow was to find the center slice through the reconstruction, which was done for the binarized data and then applied to the nonbinarized data (before segmentation). Thereby, we ensured that the fitting was performed along the smallest gap distance. The position of the line profile was determined by applying the EEDT to the binarized data, which identified the z and y coordinates of the closest two pixels. From these closest pixels, line profiles were extracted along the x direction, i.e., the gap direction. To account for local variations in the gap region, the position of the line profile was shifted within a range of ± 3 pixels in each direction around the smallest distance between the two closest pixels (see Fig. S6(a) in the Supplemental Material [60]). The fitting procedure was performed on the average line profile (Fig. S6(b) in the Supplemental Material [60]). It should be

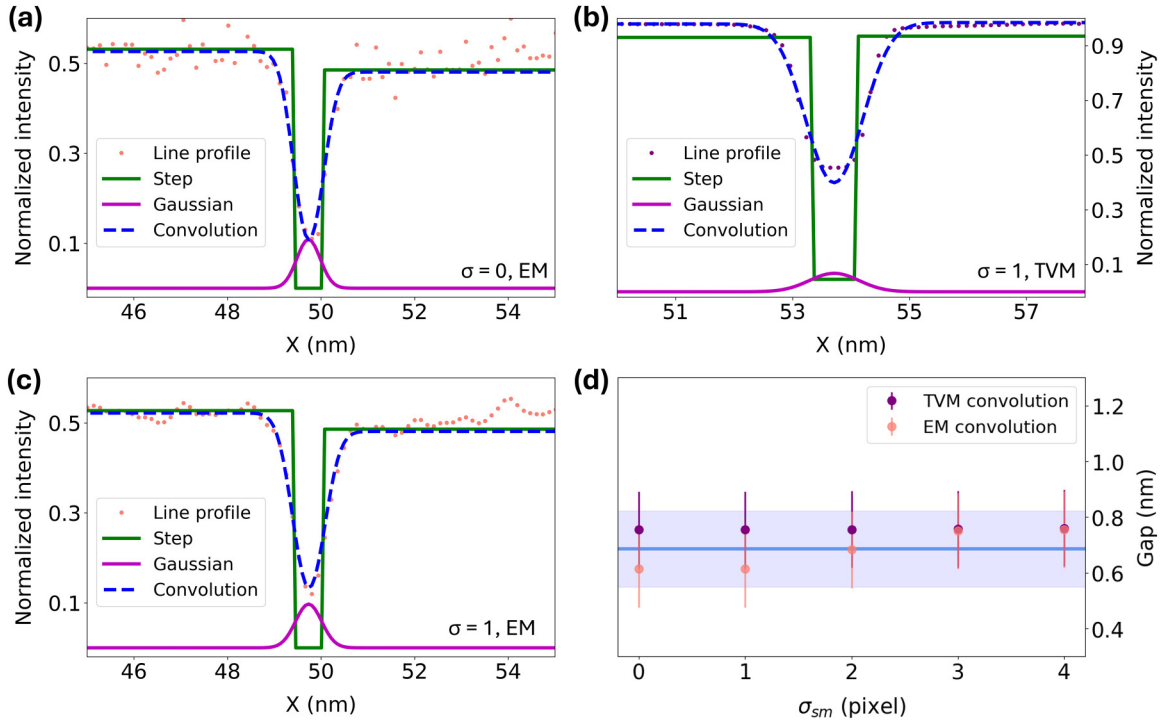


FIG. 3. Convolution fit applied to the simulated series of a dimer, reconstructed using the EM (salmon) and TVM (purple) algorithms. A representative convolution fit is illustrated for the EM reconstruction with applied smoothing of $\sigma_{sm} = 0$ in (a) and $\sigma_{sm} = 1$ in (c). In (b), a representative convolution fit is shown for the TVM reconstruction with applied smoothing $\sigma_{sm} = 1$. In (d), the extracted gap from each fit is plotted in salmon (EM reconstruction) and purple (TVM reconstruction) after applying different levels of smoothing. The ground truth for the simulated known gap (0.68 nm) is represented by the blue line. The light blue region indicates the tolerance corresponding to the pixel size ± 1 .

noted that this approach might lead to misestimation of the gap direction in case of significant size differences between NPs and/or highly uneven substrates, where the gap is no longer aligned along one of the axes. For the NP sizes and substrates analyzed in this work, the gap direction was always along the x axis, but the approach proposed here is straightforward to generalize to arbitrary gap directions.

The next step in the procedure was fitting the average line profile with a convolution of a step function and a Gaussian function. It should be noted that noise in the reconstruction might lead to small differences in the average intensity on both sides of the gap. We thus allowed the step function to have different heights on both sides of the gap. To improve the convergence of the fitting, we estimated the initial parameters by fitting two logistic functions independently to both sides of the gap, as shown in Fig. S6(c) in the Supplemental Material [60]. The fitting process was carried out using the least squares minimization method. Details can be found in Sec. II H.

Tilt series of HAADF-STEM data were simulated for different dimer configurations including realistic experimental noise to test this workflow (see Sec. II E for details). The first system consisted of two perfect spheres (Fig. S13 in the Supplemental Material [60]), each with a radius of 23 nm and a gap size varying between 1.09 nm (upper row in Fig. S13) and 0.55 nm (lowest row in Fig. S13). The second configuration was a dimer with one sphere of 23 nm radius and the other of 30 nm radius, separated by a gap of 0.82 nm (middle row in Fig. S13). These initial tests demonstrated

that our fitting procedure could reliably reproduce the size of the gap with one pixel accuracy, regardless of the smoothing strength of the reconstructions or whether they were equally and nonequally sized particles (see Fig. S13 in the Supplemental Material [60]). The fit results clearly produced more accurate estimates than the classic Otsu segmentation, which completely failed for very small gap sizes (Fig. S13(c.3) in the Supplemental Material [60]) as well as for $\sigma_{sm} = 0$ and $\sigma_{sm} > 3$.

Since experimental systems are unlikely to be perfectly spherical particles, we also generated a model system based on a more realistic shape. To account for asymmetries and deviations from ideal spherical shapes, we used the segmented 3D structure based on experimental results as the ground truth. Using this segmented ground truth, we simulated an HAADF-STEM tilt series (as detailed in Sec. II E) to evaluate the suitability of the proposed convolution model. The initially segmented gap size of the voxelized structure, which was 0.68 nm for this specific reconstruction, served as the reference. We already know that this is not the accurate gap size of the experimental data, but it only serves here as a known ground truth to test our fitting approach on a more realistic structure. Like Fig. 2, we applied different reconstruction algorithms and smoothing strengths σ_{sm} to the reconstructed dataset before the fit. In Fig. 3(a), the averaged line profile along the direction of the smallest gap of the EM reconstruction for this generated ground truth is shown, along with the fitted function for $\sigma_{sm} = 0$ (no additional smoothing). The fit results for $\sigma_{sm} = 1$ for the TVM and EM reconstructions

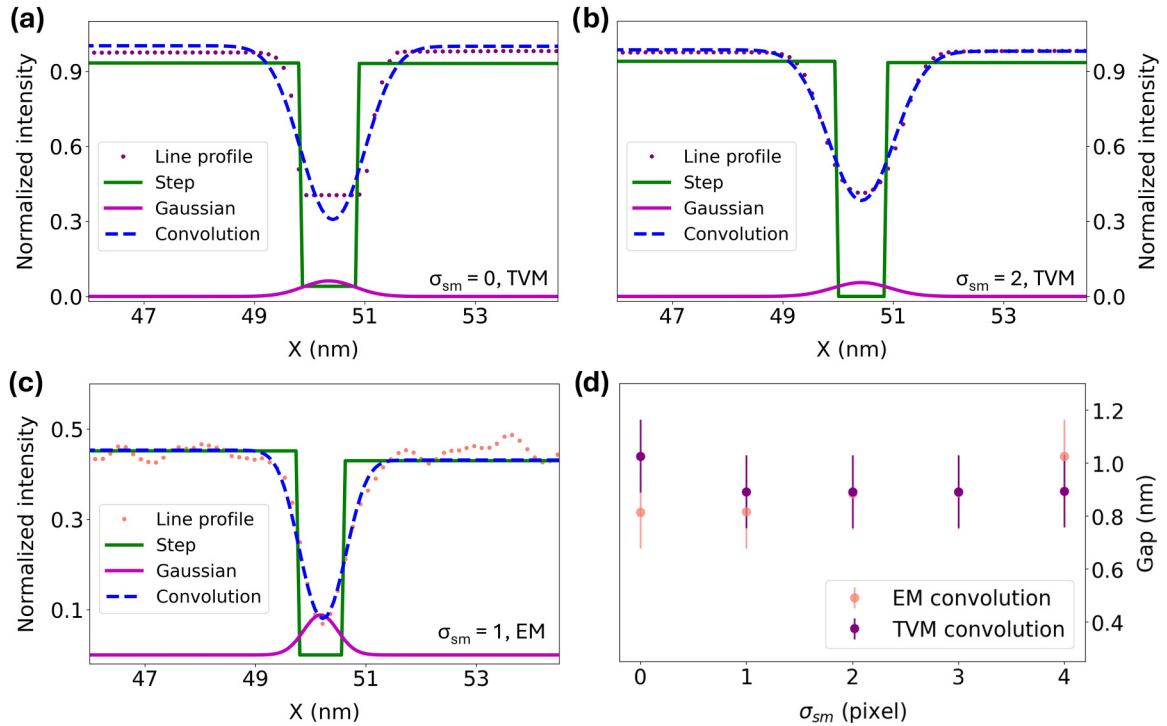


FIG. 4. Convolution fit applied to the experimental series reconstructed using EM (salmon) and TVM (purple) algorithms. A representative convolution fit is illustrated for the TVM reconstruction with applied smoothing $\sigma_{sm} = 0$ in (a) and $\sigma_{sm} = 2$ in (b). In (c), a representative convolution fit is shown for the EM reconstruction with applied smoothing $\sigma_{sm} = 1$. The extracted gap sizes for each fit are summarized in (d).

are displayed in Figs. 3(b) and 3(c), respectively. Figure 3(d) shows the extracted gap size from each fit. Unlike the results obtained without fitting shown in Fig. 2, the fitted gap size is insensitive to additional data preprocessing. Moreover, for every σ_{sm} , we could extract the expected gap size (straight blue line) within the accuracy of ± 1 pixel (± 0.14 nm, light blue box). The error was dominated by the pixel size and error propagation from the fit barely increased it. Therefore, our fitting approach offers a simple and reliable method to extract the gap size that is independent of the data processing pipeline before fitting. Furthermore, it can be applied to any particle geometry, as it does not require prior knowledge of the particle shape, as shown in Fig. 3. It should be noted that this works particularly well if the gap is not located along the direction of the missing wedge. Thus, an optimal alignment of the dimer system before acquiring a tomography series is essential for achieving the most reliable results.

C. Convolution on experimental data

Once the model was successfully validated on simulated data, we applied it to the experimental reconstructions from Fig. 2. As shown in Fig. 4, the model performed well on experimental data, both for the TVM, Figs. 4(a) and 4(b), and the EM reconstructions, Fig. 4(c). Independent of the preprocessing, i.e., the reconstruction algorithm or applied smoothing parameter σ_{sm} , we extracted a very similar gap size, as shown in Fig. 4(d). Excluding the gap size extracted from TVM for $\sigma_{sm} = 0$, the maximum difference in gap sizes from the different fits was found to be 0.074 nm, which is only half of the pixel size. Small discrepancies in gap size arose

for $\sigma_{sm} = 0$ and large Gaussian blurring values ($\sigma_{sm} = 4$) for similar reasons as discussed in Fig. 2. For $\sigma_{sm} = 0$, single voxel protrusions due to the nonsmoothed noise likely also caused the larger fitting error for the extracted gap size for EM. For TVM, the cause of the larger deviation for $\sigma_{sm} = 0$ was the intensity plateau in the gap region due to the nature of the algorithm, which caused a mismatch with our model as seen in Fig. 4(a). As shown in Fig. 4(b), this problem did not occur for larger nonzero σ_{sm} . It is therefore advisable to use slight smoothing of the reconstruction to avoid the different effects for the different reconstructions. Nonetheless, for all the different processing parameters, we extracted a gap size within the pixel error. By averaging the gap values from the TVM and EM reconstructions for $\sigma_{sm} = 1, 2$, and 3, an average gap size of 0.87 nm was obtained. This result is in excellent agreement with computational work on calculating the length of the BDT molecules between gold atoms, which resulted in 0.84–0.85 nm [69,70].

As explained earlier, a surface mesh is required as input for BEM to simulate the optical properties. In the discussion surrounding Fig. 2, the mesh determination was highly uncertain due to ambiguities about the gap size. Due to the robustness of the convolution fit, we can now take the average fitted gap size (0.87 nm for this system) as the ground truth and adjust the surface mesh such that it matches the fitted gap size. To achieve this, the reconstruction was first segmented. For that, we can again make use of our fit since the threshold value can be estimated as the intercept of the convolution curve with the step function. In the following, we will refer to this as threshold fraction $\theta_t = 1$. A representative example of the identification of θ_t is shown in Fig. S6(d) in the Supplemental

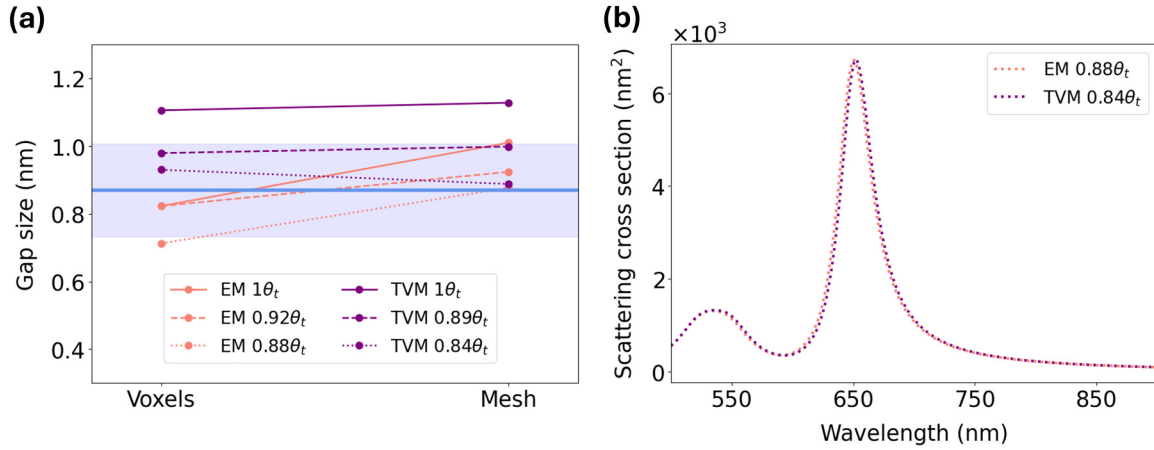


FIG. 5. (a) Comparison of the gap extracted using the EEDT applied to the voxelized data before (voxels) and after meshing for different fraction of θ_t , where $\theta_t = 1$ correspond to the threshold obtained from the fit. (b) Comparison of simulated scattering spectra for the meshed EM and TVM reconstructions for the same gap size after meshing.

Material [60]. It is important to note, as discussed previously, that the mesh simplification unavoidably introduces slight deviations in the morphology. Since the scattering response of dimers is highly sensitive to sub-nanometer variations in the gap size, these differences can significantly impact the final results. Therefore, to accurately interpret the scattering spectra, it is essential to ensure that the gap size is the same as that obtained from the convolution fit after meshing and mesh simplification. Therefore, we compared the gap size after segmentation based on the threshold obtained from the convolution fit and after subsequent meshing and mesh simplification.

In Fig. 5(a), the gap sizes extracted before and after meshing, calculated by applying the EEDT, are reported for different fractions of the convolution fit intercept threshold θ_t . As suspected, the gap changed after meshing, which was even on the order of 0.2 nm in some cases. We noticed that the size of the retrieved gap was systematically increasing for EM reconstructions. On the contrary, for the TVM reconstructions, the gap size was reduced or remained invariant. It should be noted that changes in gap size can only be avoided for a very large number of faces, which makes any electromagnetic simulations unfeasible. To estimate the effect of the number of faces on the gap size, we simplified the meshes to different numbers of faces (Fig. S14 in the Supplemental Material [60]). We only saw a deviation for a very small number of faces (1000) and observed no changes for 6000 faces (used for the simulations here) until 10 000 faces.

To avoid these issues, we propose an alternative solution: The threshold value for the segmentation shall be fine-tuned such that the gap size after meshing and mesh simplification aligns with the value obtained from the fit, now considered as the ground truth. As previously described, the gap size from the fit was determined to be 0.87 nm by taking the average of the value extracted from the fit for EM and TVM reconstructions smoothed with a σ_{sm} ranging from 1 to 3. In Fig. 5(a), the different lines correspond to variations in this threshold value relative to the initial value θ_t obtained from the fit. For the studied dimer, the fitted gap size could be recovered after meshing for a relative threshold value of $0.88\theta_t$ and

$0.84\theta_t$ for the EM and TVM reconstructions, respectively. The corresponding calculated scattering spectra are shown in Fig. 5(b). The spectra overlap nicely, indicating that this approach resulted in a good mesh representation of the morphology and is a robust method for calculating the optical response of a dimer of gold NPs independent of the exact preprocessing parameters. Because of the missing wedge effect, the volume of the EM reconstruction was slightly bigger than for the TVM reconstruction, a reproducible trend for any fraction of θ_t (Fig. S15(a) in the Supplemental Material [60]). As expected for spherical particles, this volume difference did not seem to modify the scattering response significantly, which we believe to be therefore dominated by the gap size after meshing. This is further demonstrated in Figs. S15(b) and S15(c) in the Supplemental Material [60], where an increasing fraction of θ_t led to a gradual blueshift due to an increase in gap size (Fig. S15(a) in the Supplemental Material [60]). The overlap of the simulated spectra based on EM and TVM reconstructions—when matching the gap size after meshing—could also be reproduced for the simulated data, where the calculated ground truth spectrum overlaps with those from the reconstructions (Fig. S16 in the Supplemental Material [60]). This provides additional proof that, with our workflow, accurate simulated electromagnetic spectra can be obtained without uncertainties about the morphology of the input structure. This, in turn, enables careful comparisons with experimental spectra in the future, making it possible to fingerprint quantum effects in these systems.

IV. CONCLUSIONS

In this work, we first highlighted the limitations of 2D (S)TEM imaging in accurately segmenting sub-nanometer features, such as the interparticle gaps in plasmonic nanosphere dimers studied here. We demonstrated that ET significantly improved segmentation accuracy but introduced uncertainties related to data processing. Specifically, the extracted gap size depended on the chosen reconstruction algorithm and the degree of smoothing applied. To address these challenges, we developed an optimal workflow for extracting sub-nanometer gaps and converting the 3D data into a

reliable surface mesh. We found that fitting a convolution of a step function and a Gaussian function to line profiles from tomography reconstructions produced consistent gap size measurements. We validated this method using simulated data and successfully retrieved the known ground truth gap sizes with a pixel size level of accuracy (0.14 nm in our case). Once the gap size was accurately estimated from fitting, we adjusted the segmentation threshold in the tomography reconstruction to ensure that the gap size was preserved upon meshing and mesh simplification. The resulting surface mesh was used for electromagnetic simulations of the optical response of the gold dimer. We believe this approach is broadly applicable to various gap sizes and material systems. Furthermore, reducing the pixel size in experiments can further minimize the error in gap size estimation. Accurately simulating the optical

properties of nanoscale systems with sub-nanometer precision will ultimately enable the design of plasmonic structures with finely tuned optical properties, optimizing their performance for specific functions. This capability is particularly important for applications in catalysis, sensing, and quantum optics.

ACKNOWLEDGMENT

This work was part of the research program of AMOLF, which is partly financed by the Dutch Research Council.

DATA AVAILABILITY

The data that support the findings of this article are openly available [75].

- [1] P. Zijlstra, M. Orrit, and A. F. Koenderink, Metal nanoparticles for microscopy and spectroscopy, in *Nanoparticles: Workhorses of Nanoscience*, edited by C. de Mello Donegá (Springer, Berlin, 2014), pp. 53–98.
- [2] J. N. Anker, W. P. Hall, O. Lyandres, N. C. Shah, J. Zhao, and R. P. Van Duyne, Biosensing with plasmonic nanosensors, *Nat. Mater.* **7**, 442 (2008).
- [3] W. Fan, B. J. Lawrie, and R. C. Pooser, Quantum plasmonic sensing, *Phys. Rev. A* **92**, 053812 (2015).
- [4] A. B. Taylor and P. Zijlstra, Single-molecule plasmon sensing: Current status and future prospects, *ACS Sensors* **2**, 1103 (2017).
- [5] E. Mauriz and L. M. Lechuga, Plasmonic biosensors for single-molecule biomedical analysis, *Biosensors* **11**, 123 (2021).
- [6] N. G. Khlebtsov and L. A. Dykman, Optical properties and biomedical applications of plasmonic nanoparticles, *J. Quant. Spectrosc. Radiat. Transfer* **111**, 1 (2010).
- [7] H. Liao, C. L. Nehl, and J. H. Hafner, Biomedical applications of plasmon resonant metal nanoparticles, *Nanomedicine* **1**, 201 (2006).
- [8] G. Y. Yi, M. J. Kim, H. I. Kim, J. Park, and S. H. Baek, Hyperthermia treatment as a promising anti-cancer strategy: Therapeutic targets, perspective mechanisms and synergistic combinations in experimental approaches, *Antioxidants* **11**, 625 (2022).
- [9] M. Ravichandran, G. Oza, S. Velumani, J. T. Ramirez, F. Garcia-Sierra, N. B. Andrade, A. Vera, L. Leija, and M. A. Garza-Navarro, Plasmonic/magnetic multifunctional nanoplat-form for cancer theranostics, *Sci. Rep.* **6**, 34874 (2016).
- [10] J. B. Sambur and P. Chen, Approaches to single-nanoparticle catalysis, *Annu. Rev. Phys. Chem.* **65**, 395 (2014).
- [11] S. Yu, A. J. Wilson, G. Kumari, X. Zhang, and P. K. Jain, Opportunities and challenges of solar-energy-driven carbon dioxide to fuel conversion with plasmonic catalysts, *ACS Energy Lett.* **2**, 2058 (2017).
- [12] W. Hou and S. B. Cronin, A review of surface plasmon resonance-enhanced photocatalysis, *Adv. Funct. Mater.* **23**, 1612 (2013).
- [13] E. Cortés, L. V. Besteiro, A. Alabastri, A. Baldi, G. Tagliabue, A. Demetriadou, and P. Narang, Challenges in plasmonic catalysis, *ACS Nano* **14**, 16202 (2020).
- [14] K. Sytwu, M. Vadai, and J. A. Dionne, Bimetallic nanostructures: Combining plasmonic and catalytic metals for photocatalysis, *Adv. Phys.: X* **4**, 1619480 (2019).
- [15] C. C. Carlin, A. X. Dai, A. Al-Zubeidi, E. M. Simmerman, H. Oh, N. Gross, S. A. Lee, S. Link, C. F. Landes, F. H. da Jornada *et al.*, Nanoscale and ultrafast *in situ* techniques to probe plasmon photocatalysis, *Chem. Phys. Rev.* **4**, 041309 (2023).
- [16] K. L. Kelly, E. Coronado, L. L. Zhao, and G. C. Schatz, The optical properties of metal nanoparticles: The influence of size, shape, and dielectric environment, *J. Phys. Chem. B* **107**, 668 (2003).
- [17] N. Li, P. Zhao, and D. Astruc, Anisotropic gold nanoparticles: Synthesis, properties, applications, and toxicity, *Angew. Chem., Int. Ed.* **53**, 1756 (2014).
- [18] C. T. Cooper, M. Rodriguez, S. Blair, and J. S. Shumaker-Parry, Mid-infrared localized plasmons through structural control of gold and silver nanocrescents, *J. Phys. Chem. C* **119**, 11826 (2015).
- [19] A. Amirjani and S. K. Sadrnezhad, Computational electromagnetics in plasmonic nanostructures, *J. Mater. Chem. C* **9**, 9791 (2021).
- [20] M. Dieperink, A. Skorikov, N. Claes, S. Bals, and W. Albrecht, Considerations for electromagnetic simulations for a quantitative correlation of optical spectroscopy and electron tomography of plasmonic nanoparticles, *Nanophotonics* **13**, 4647 (2024).
- [21] U. Hohenester and A. Trügler, MNPBEM—A MATLAB toolbox for the simulation of plasmonic nanoparticles, *Comput. Phys. Commun.* **183**, 370 (2012).
- [22] N. A. Mortensen, Mesoscopic electrodynamics at metal surfaces—From quantum-corrected hydrodynamics to microscopic surface-response formalism, *Nanophotonics* **10**, 2563 (2021).
- [23] M. S. Tame, K. McEnery, Ş. Özdemir, J. Lee, S. A. Maier, and M. Kim, Quantum plasmonics, *Nat. Phys.* **9**, 329 (2013).
- [24] J. M. Fitzgerald, P. Narang, R. V. Craster, S. A. Maier, and V. Giannini, Quantum plasmonics, *Proc. IEEE* **104**, 2307 (2016).
- [25] J. A. Scholl, A. L. Koh, and J. A. Dionne, Quantum plasmon resonances of individual metallic nanoparticles, *Nature (London)* **483**, 421 (2012).

- [26] Z. Jacob and V. M. Shalae, Plasmonics goes quantum, *Science* **334**, 463 (2011).
- [27] Z.-K. Zhou, J. Liu, Y. Bao, L. Wu, C. E. Png, X.-H. Wang, and C.-W. Qiu, Quantum plasmonics get applied, *Prog. Quantum Electron.* **65**, 1 (2019).
- [28] D. Xu, X. Xiong, L. Wu, X.-F. Ren, C. E. Png, G.-C. Guo, Q. Gong, and Y.-F. Xiao, Quantum plasmonics: New opportunity in fundamental and applied photonics, *Adv. Opt. Photon.* **10**, 703 (2018).
- [29] D. C. Marinica, M. Zapata, P. Nordlander, A. K. Kazansky, P. M. Echenique, J. Aizpurua, and A. G. Borisov, Active quantum plasmonics, *Sci. Adv.* **1**, e1501095 (2015).
- [30] Y. Luo, A. I. Fernandez-Dominguez, A. Wiener, S. A. Maier, and J. B. Pendry, Surface plasmons and nonlocality: A simple model, *Phys. Rev. Lett.* **111**, 093901 (2013).
- [31] S. Raza, S. I. Bozhevolnyi, M. Wubs, and N. A. Mortensen, Nonlocal optical response in metallic nanostructures, *J. Phys.: Condens. Matter* **27**, 183204 (2015).
- [32] M. Kauranen and A. V. Zayats, Nonlinear plasmonics, *Nat. Photon.* **6**, 737 (2012).
- [33] N. C. Panou, W. E. Sha, D. Lei, and G. Li, Nonlinear optics in plasmonic nanostructures, *J. Opt.* **20**, 083001 (2018).
- [34] M. Mesch, B. Metzger, M. Hentschel, and H. Giessen, Nonlinear plasmonic sensing, *Nano Lett.* **16**, 3155 (2016).
- [35] R. Esteban, A. G. Borisov, P. Nordlander, and J. Aizpurua, Bridging quantum and classical plasmonics with a quantum-corrected model, *Nat. Commun.* **3**, 825 (2012).
- [36] A. Varas, P. García-González, J. Feist, F. García-Vidal, and A. Rubio, Quantum plasmonics: From jellium models to *ab initio* calculations, *Nanophotonics* **5**, 409 (2016).
- [37] N. Zohar, L. Chuntonov, and G. Haran, The simplest plasmonic molecules: Metal nanoparticle dimers and trimers, *J. Photochem. Photobiol. C* **21**, 26 (2014).
- [38] P. Nordlander, C. Oubre, E. Prodan, K. Li, and M. Stockman, Plasmon hybridization in nanoparticle dimers, *Nano Lett.* **4**, 899 (2004).
- [39] C. P. Byers, H. Zhang, D. F. Swearer, M. Yorulmaz, B. S. Hoener, D. Huang, A. Hoggard, W.-S. Chang, P. Mulvaney, E. Ringe *et al.*, From tunable core-shell nanoparticles to plasmonic drawbridges: Active control of nanoparticle optical properties, *Sci. Adv.* **1**, e1500988 (2015).
- [40] R. Esteban, G. Aguirregabiria, A. G. Borisov, Y. M. Wang, P. Nordlander, G. W. Bryant, and J. Aizpurua, The morphology of narrow gaps modifies the plasmonic response, *ACS photon.* **2**, 295 (2015).
- [41] C. Ciraci, R. Hill, J. Mock, Y. Urzhumov, A. Fernández-Domínguez, S. Maier, J. Pendry, A. Chilkoti, and D. Smith, Probing the ultimate limits of plasmonic enhancement, *Science* **337**, 1072 (2012).
- [42] T. V. Teperik, P. Nordlander, J. Aizpurua, and A. G. Borisov, Robust subnanometric plasmon ruler by rescaling of the nonlocal optical response, *Phys. Rev. Lett.* **110**, 263901 (2013).
- [43] K. J. Savage, M. M. Hawkeye, R. Esteban, A. G. Borisov, J. Aizpurua, and J. J. Baumberg, Revealing the quantum regime in tunneling plasmonics, *Nature (London)* **491**, 574 (2012).
- [44] O. Pérez-González, N. Zabala, A. G. Borisov, N. J. Halas, P. Nordlander, and J. Aizpurua, Optical spectroscopy of conductive junctions in plasmonic cavities, *Nano Lett.* **10**, 3090 (2010).
- [45] J. A. Scholl, A. García-Etxarri, A. L. Koh, and J. A. Dionne, Observation of quantum tunneling between two plasmonic nanoparticles, *Nano Lett.* **13**, 564 (2013).
- [46] H. Cha, J. H. Yoon, and S. Yoon, Probing quantum plasmon coupling using gold nanoparticle dimers with tunable interparticle distances down to the subnanometer range, *ACS Nano* **8**, 8554 (2014).
- [47] F. Benz, C. Tserkezis, L. O. Herrmann, B. De Nijs, A. Sanders, D. O. Sigle, L. Pukenas, S. D. Evans, J. Aizpurua, and J. J. Baumberg, Nanooptics of molecular-shunted plasmonic nanojunctions, *Nano Lett.* **15**, 669 (2015).
- [48] S. Lerch and B. M. Reinhard, Effect of interstitial palladium on plasmon-driven charge transfer in nanoparticle dimers, *Nat. Commun.* **9**, 1608 (2018).
- [49] S. F. Tan, L. Wu, J. K. Yang, P. Bai, M. Bosman, and C. A. Nijhuis, Quantum plasmon resonances controlled by molecular tunnel junctions, *Science* **343**, 1496 (2014).
- [50] D. Knebl, A. Hörl, A. Trügler, J. Kern, J. R. Krenn, P. Puschnig, and U. Hohenester, Gap plasmonics of silver nanocube dimers, *Phys. Rev. B* **93**, 081405(R) (2016).
- [51] W. Yan, M. Wubs, and N. A. Mortensen, Projected dipole model for quantum plasmonics, *Phys. Rev. Lett.* **115**, 137403 (2015).
- [52] K. Jenkinson, L. M. Liz-Marzán, and S. Bals, Multimode electron tomography sheds light on synthesis, structure, and properties of complex metal-based nanoparticles, *Adv. Mater.* **34**, 2110394 (2022).
- [53] P. A. Midgley and M. Weyland, 3D electron microscopy in the physical sciences: The development of Z-contrast and electron tomography, *Ultramicroscopy* **96**, 413 (2003).
- [54] W. Albrecht and S. Bals, Fast electron tomography for nanomaterials, *J. Phys. Chem. C* **124**, 27276 (2020).
- [55] S. Hata, H. Furukawa, T. Gondo, D. Hirakami, N. Horii, K. I. Ikeda, K. Kawamoto, K. Kimura, S. Matsumura, M. Mitsuhara *et al.*, Electron tomography imaging methods with diffraction contrast for materials research, *Microscopy* **69**, 141 (2020).
- [56] B. Goris, T. Roelandts, K. J. Batenburg, H. H. Mezerji, and S. Bals, Advanced reconstruction algorithms for electron tomography: From comparison to combination, *Ultramicroscopy* **127**, 40 (2013).
- [57] S. Triviño-Sánchez, R. Xu, J. González-Izquierdo, L. Bañares, I. Cano, J. Pérez-Juste, A. Guerrero-Martínez, and G. González-Rubio, Colloidal gold-palladium-platinum alloy nanospheres with tunable compositions and defined numbers of atoms, *Nanoscale* **17**, 8577 (2025).
- [58] G. Gonzalez-Rubio, P. Llombart, J. Zhou, H. Geiss, O. Peña-Rodríguez, H. Gai, B. Ni, R. Rosenberg, and H. Cölfen, Revisiting the role of seed size for the synthesis of highly uniform sub-10 nm length gold nanorods, *Chem. Mater.* **36**, 1982 (2024).
- [59] A.-K. Göppert, G. Gonzalez-Rubio, S. Schnitzlein, and H. Cölfen, A nanoparticle-based model system for the study of heterogeneous nucleation phenomena, *Langmuir* **39**, 3580 (2023).
- [60] See Supplemental Material at <http://link.aps.org/supplemental/10.1103/9jvw-qdsx> for details on sample preparation and the workflow for simulating the tomography series. A detailed comparison of mesh quality using the fast simplification algorithm and ACVD is provided, together with the impact on simulated optical properties. Details on the fitting procedure are included with a figure showing the extracted sigma values

from the fit; examples of line profiles, logistic function fitting, and threshold value extraction; and a table summarizing the initial fit parameters. Details on the procedure for gap size extraction from meshes and voxelized structure are provided. The stability of the system under an electron beam is proved by showing tomography reconstructions from two series acquired consecutively on the same dimer. The gap extraction fit is further validated on additional simulated data. Additional scattering spectra are shown to illustrate the influence of different parameters—volume, gap and mesh quality—on the optical response of dimers, both in simulations and experimental reconstructions.

- [61] W. Van den Broek, A. Rosenauer, B. Goris, G. Martinez, S. Bals, S. Van Aert, and D. Van Dyck, Correction of non-linear thickness effects in HAADF STEM electron tomography, *Ultramicroscopy* **116**, 8 (2012).
- [62] W. van Aarle, W. J. Palenstijn, J. De Beenhouwer, T. Altantzis, S. Bals, K. J. Batenburg, and J. Sijbers, The ASTRA toolbox: A platform for advanced algorithm development in electron tomography, *Ultramicroscopy* **157**, 35 (2015).
- [63] E. Y. Sidky, J. H. Jørgensen, and X. Pan, Convex optimization problem prototyping for image reconstruction in computed tomography with the Chambolle-Pock algorithm, *Phys. Med. Biol.* **57**, 3065 (2012).
- [64] A. Paszke, S. Gross, F. Massa, A. Lerer, J. Bradbury, G. Chanan, T. Killeen, Z. Lin, N. Gimelshein, L. Antiga *et al.*, PyTorch: An imperative style, high-performance deep learning library, *Advances in neural information processing systems* 32 (2019).
- [65] S. van der Walt, J. L. Schönberger, J. Nunez-Iglesias, F. Boulogne, J. D. Warner, N. Yager, E. Gouillart, and T. Yu, scikit-image: Image processing in Python, *PeerJ* **2**, e453 (2014).
- [66] W. E. Lorensen and H. E. Cline, Marching cubes: A high resolution 3D surface construction algorithm, in *Proceedings of the 14th Annual Conference on Computer Graphics and Interactive Techniques, SIGGRAPH '87* (Association for Computing Machinery, New York, 1987), pp. 163–169.
- [67] S. Valette, J. M. Chassery, and R. Prost, Generic remeshing of 3D triangular meshes with metric-dependent discrete voronoi diagrams, *IEEE Trans. Visual Comput. Graphics* **14**, 369 (2008).
- [68] K. M. McPeak, S. V. Jayanti, S. J. P. Kress, S. Meyer, S. Iotti, A. Rossinelli, and D. J. Norris, Plasmonic films can easily be better: Rules and recipes, *ACS Photon.* **2**, 326 (2015).
- [69] M. A. Reed, C. Zhou, C. Muller, T. Burgin, and J. Tour, Conductance of a molecular junction, *Science* **278**, 252 (1997).
- [70] Y. Kim, T. Pietsch, A. Erbe, W. Belzig, and E. Scheer, Benzenedithiol: A broad-range single-channel molecular conductor, *Nano Lett.* **11**, 3734 (2011).
- [71] J. Zheng, J. Liu, Y. Zhuo, R. Li, X. Jin, Y. Yang, Z.-B. Chen, J. Shi, Z. Xiao, W. Hong, and Z.-q. Tian, Electrical and SERS detection of disulfide-mediated dimerization in single-molecule benzene-1,4-dithiol junctions, *Chem. Sci.* **9**, 5033 (2018).
- [72] C. Glasbey, An analysis of histogram-based thresholding algorithms, *CVGIP: Graphical Models and Image Processing* **55**, 532 (1993).
- [73] N. Otsu, A threshold selection method from gray-level histograms, *IEEE Trans. Syst., Man, Cybernetics* **9**, 62 (1979).
- [74] H. H. Mezerji, W. Van den Broek, and S. Bals, A practical method to determine the effective resolution in incoherent experimental electron tomography, *Ultramicroscopy* **111**, 330 (2011).
- [75] doi: [10.5281/zenodo.16983635](https://doi.org/10.5281/zenodo.16983635)

Correction: An error in the order of author names has been fixed and the presentation of the bylines has been adjusted to accommodate for the change.